

Breaking beta: a comparison of mass modelling methods for spherical systems

J. I. Read¹,^{1*} G. A. Mamon², E. Vasiliev^{3,4,5}, L. L. Watkins^{6,7,8}, M. G. Walker⁹, J. Peñarrubia¹⁰, M. Wilkinson¹¹, W. Dehnen^{11,12} and P. Das^{1,4}

¹Department of Physics, University of Surrey, Guildford GU2 7XH, UK

²Institut d'Astrophysique de Paris (UMR 7095: CNRS & Sorbonne Université), F-75014 Paris, France

³Institute of Astronomy, University of Cambridge, Madingley Road, Cambridge CB3 0HA, UK

⁴Rudolf Peierls Centre for Theoretical Physics, University of Oxford, Oxford OX1 3NP, UK

⁵Lebedev Physical Institute, Leninsky Prospekt 53, Moscow 119991, Russia

⁶AURA for the European Space Agency (ESA), ESA Office, Space Telescope Science Institute, 3700 San Martin Drive, Baltimore, MD 21218, USA

⁷European Southern Observatory, Karl-Schwarzschild-Straße 2, D-85748 Garching bei München, Germany

⁸Department of Astrophysics, University of Vienna, Türkenschanzstraße 17, A-1180 Vienna, Austria

⁹McWilliams Center for Cosmology, Department of Physics, Carnegie Mellon University, Pittsburgh, PA 15213, USA

¹⁰Institute for Astronomy, University of Edinburgh, Blackford Hill, Edinburgh EH9 3HJ, UK

¹¹Department of Physics & Astronomy, University of Leicester, Leicester LE1 7RH, UK

¹²Universitäts-Sternwarte der Ludwig-Maximilians-Universität, Scheinerstrasse 1, D-81679 München, Germany

Accepted 2020 November 17. Received 2020 November 17; in original form 2019 December 20

ABSTRACT

We apply four different mass modelling methods to a suite of publicly available mock data for spherical stellar systems. We focus on the recovery of the density and velocity anisotropy as a function of radius, either using line-of-sight velocity data only or adding proper motion data. All methods perform well on isotropic and tangentially anisotropic mock data, recovering the density and velocity anisotropy within their 95 per cent confidence intervals over the radial range $0.25 < R/R_{1/2} < 4$, where $R_{1/2}$ is the half-light radius. However, radially anisotropic mocks are more challenging. For line-of-sight data alone, only methods that use information about the shape of the velocity distribution function are able to break the degeneracy between the density profile and the velocity anisotropy, β , to obtain an unbiased estimate of both. This shape information can be obtained through directly fitting a global phase-space distribution function, by using higher order ‘virial shape parameters’ or by assuming a Gaussian velocity distribution function locally, but projecting it self-consistently along the line of sight. Including proper motion data yields further improvements, and in this case, all methods give a good recovery of both the radial density and velocity anisotropy profiles.

Key words: galaxies: dwarf – galaxies: general – galaxies: haloes – galaxies: kinematics and dynamics – cosmology: dark matter.

1 INTRODUCTION

Many stellar systems are spherical or mildly triaxial, from globular clusters (White & Shawl 1987) and tiny gas-poor dwarf spheroidal galaxies (Sanders & Evans 2017) to giant elliptical galaxies (Hubble 1926) and even galaxy clusters (e.g. Limousin et al. 2013). Building mass models of such systems has a wide range of astrophysical applications, from hunting for intermediate-mass and supermassive black holes (e.g. Verolme et al. 2002; Noyola, Gebhardt & Bergmann 2008; van der Marel & Anderson 2010; Vitral & Mamon 2020) to probing the nature of dark matter (DM; e.g. Walker & Peñarrubia 2011; Read, Walker & Steger 2018, 2019), the stellar mass function (e.g. Cappellari et al. 2012), or the orbital velocity anisotropy (e.g. Mamon et al. 2019). The velocity anisotropy is an interesting quantity to determine as it encodes information about the assembly history of the system (e.g. Eggen, Lynden-Bell & Sandage 1962). For spherical

systems, it is typically described by the ‘anisotropy parameter’

$$\beta(r) = 1 - \frac{\sigma_{\theta}^2(r)}{\sigma_r^2(r)}, \quad (1)$$

where r is the spherically symmetric radial coordinate, $\sigma_{\theta}(r)$ is the tangential velocity dispersion, $\sigma_r(r)$ is the radial velocity dispersion, and $\beta(r) = 1$ for radial orbits, 0 for isotropic orbits, and $\beta(r) \rightarrow -\infty$ for circular orbits.

In all of the above applications, we would like to understand how model biases and systematic errors impact the results. Mock data – a dynamically realistic representation of the real data for which we know the true answer – provide an elegant way to address these questions. Such mocks can be very simple, reproducing all of the assumptions employed in the analysis of real data, or highly sophisticated, simulating the effect of data selection and/or departures from key model assumptions. For the latter, developing the mock can be a substantial task in its own right, discouraging broad and deep tests of our methodologies.

* E-mail: j.read@surrey.ac.uk

The goal of this article is to compare how four different mass-orbit modelling algorithms, applied to mock data for a spherical, single-component, dwarf galaxy, recover the radial profiles of total density and velocity anisotropy. We focus on specific physical radii, $R = [0.25, 0.5, 1, 2, 4] R_{1/2}$, where $R_{1/2}$ is the projected half-light radius of the tracer stars, and we consider both line-of-sight (LOS) velocity data for 1000 and 10 000 tracer stars¹ and proper motion data for 1000 stars. The LOS data are similar to the state-of-the-art data that are currently available for nearby dwarf galaxies (e.g. Walker, Mateo & Olszewski 2009), globular clusters (e.g. Watkins et al. 2015a; Kamann et al. 2018), giant elliptical galaxies (e.g. Napolitano et al. 2014), and clusters of galaxies [with large spectroscopic surveys such as Sloan Digital Sky Survey (York et al. 2000) and Galaxy and Mass Assembly survey (Robotham et al. 2010)]. The proper motion data are similar to what is available for globular clusters (e.g. Bellini et al. 2014; Watkins et al. 2015b; Zocchi, Gieles & Hénault-Brunet 2017) and what will hopefully become available for dwarf galaxies from future planned missions (e.g. Strigari, Bullock & Kaplinghat 2007; Theia Collaboration 2017; Massari et al. 2018, 2020).

Our mock data suite is publicly available on the *Gaia* Challenge wiki site² and has already been used to test a number of methods in the literature (Walker & Peñarrubia 2011; Richardson & Fairbairn 2014; Bonnavard et al. 2015; Geringer-Sameth, Koushiappas & Walker 2015; Genina & Fairbairn 2016; Zhu et al. 2016; Chiappo et al. 2017; Read & Steger 2017; Diakogiannis et al. 2019). These mock data will continue to grow and improve in sophistication over time. Our central philosophy is that *it is much easier to produce a sophisticated mock than to produce a sophisticated mass modelling tool*. Using such mocks may demonstrate that simple models – e.g. those that assume spherical symmetry – work sufficiently well to test or rule out interesting models, or estimate a given parameter of interest. In this case, increasing the sophistication of the model is not required. Mock data tests can also help us identify problems in the real data – for example, if confidence intervals on the model are much smaller than those expected from the mock.

In this paper, we assess the performance of four mass modelling methods described in Section 3 through their recovery of the radial density and velocity anisotropy profiles. Three of these methods, namely GRAVSPHERE, MAMPOSST, and DISCRETEJAM, are based on the Jeans (1922) equation of local dynamical equilibrium, while one, AGAMA, is based on fitting a global distribution function (DF). For stationary spherical systems without streaming motions, the Jeans equation is given by (e.g. Binney & Tremaine 2008)

$$\frac{d(v(r)\sigma_r^2(r))}{dr} + 2\frac{\beta(r)}{r}v(r)\sigma_r^2(r) = -v(r)\frac{GM(r)}{r^2}, \quad (2)$$

where $v(r)$ is the tracer density, $M(r)$ is the total enclosed mass, $\beta(r)$ is the anisotropy parameter (1), and G is Newton’s gravitational constant. Jeans methods have the advantage that they can be efficiently implemented, allowing a wide range of models to be explored (e.g. Read & Steger 2017). Furthermore, since they do not require any assumption about the form of the DF, they can be constructed to be formally unbiased (e.g. Read 2014; Read & Steger 2017). However, disadvantages include the fact that the fits can, in principle, require a formally negative (i.e. unphysical) DF (e.g. An & Evans 2006). By contrast, methods like AGAMA have the advantage that they provide

a full DF that is positive definite and that can be easily convolved with errors, binary contamination (e.g. McConnachie & Côté 2010; Spencer et al. 2018), and survey selection functions. However, if the chosen parametrization of the DF does not contain the true solution, such methods run the risk of becoming biased (e.g. Garbari, Read & Lake 2011).

We focus here on a suite of spherical, idealized, mocks with minimal measurement uncertainties as a starting point. As we shall see, already this presents a challenge for some methods, primarily due to the mass–anisotropy degeneracy (e.g. Binney & Mamon 1982; Read & Steger 2017). More sophisticated mocks that break spherical symmetry and include the impact of unbound tidally stripped stars, lower numbers of tracer stars, and multiple independent tracer populations are also available through the *Gaia* Challenge wiki site. These have already been presented in the literature for the GRAVSPHERE method (Read & Steger 2017; Read et al. 2018; Gregory et al. 2019), with the result that – at least for 1000 tracers with small velocity uncertainties – these additional complications do not dominate the error budget. Other groups have reached similar conclusions with their own mock data tests, including cosmologically realistic mocks (e.g. Sanchis, Łokas & Mamon 2004; Wojtak et al. 2009; Kowalczyk et al. 2013; Mamon, Biviano & Boué 2013; Genina et al. 2020; Hayashi, Chiba & Ishiyama 2020). We will consider such more sophisticated tests on the methods presented here in future work.

This paper is organized as follows: In Section 2, we describe the mock data suite and how it was set up. In Section 3, we describe the different mass modelling techniques we apply to these mock data. In Section 4, we apply several modelling methods to the spherical mocks to examine the accuracy of their inferred density $\rho(r)$ and velocity anisotropy $\beta(r)$ profiles. Finally, in Section 5, we discuss our results and present our conclusions.

2 MOCK DATA

In this section, we describe our mock data; the full ‘default spherical’ suite is summarized in Table 1 and is publicly available at the *Gaia* Challenge wiki site.² All of the mock data have a single population of massless tracer stars orbiting within a host DM halo. They are available either without errors or with normally distributed errors with a standard deviation of 2 km s^{-1} on the LOS velocities for each star (larger errors can easily be added to explore their effect, but in this paper we will focus on the case where the measurement uncertainties do not dominate over the sampling error). We also include proper motion data, assuming similarly small measurement errors.

As discussed in Section 1, the *Gaia* Challenge suite also includes a host of more realistic triaxial, tidally stripped, and split-population mocks. We will consider more realistic mocks with individual star-by-star velocity errors, binary star contamination, contamination from Milky Way stars, unbound tidally stripped stars, and a realistic survey selection function in future work. We note, however, that – at least for mock galaxies similar to the Milky Way ‘classical’ dwarfs – previous works have found these additional effects to be small (e.g. Walker & Peñarrubia 2011; Laporte et al. 2013; Read et al. 2018; Genina et al. 2020).

We label the mocks using the following naming convention:

(light profile)⟨DM cusp/core⟩⟨anisotropy⟩,

where the (light profile) can be Plummer-like (Plummer 1911; Plum) or cusped (NonPlum); the DM halo can be cusped (Cusp) or cored (Core); and the ⟨anisotropy⟩ can be isotropic (Iso), of generalized

¹We define ‘tracer’ stars as massless particles orbiting in the combined gravitational potential of all stars, gas, DM, etc. in a stellar system.

²<http://astrowiki.ph.surrey.ac.uk/dokuwiki/> (under the ‘Spherical & Triaxial’ suite tab).

Table 1. Parameters of the spherical mock data that we use in this paper. The columns, from left to right, give the mock data label, the tracer density parameters (see equation 3), the DM halo density parameters (see equation 3), the velocity anisotropy profile, and the projected half-stellar mass radius. The length units are given in kpc, while ρ_0 has units of $10^7 M_\odot \text{kpc}^{-3}$. The mock labelling convention is (light profile) (cusp/core) (anisotropy), where the (light profile) can be Plummer-like (Plum; $\gamma_* = 0.1$) or cusped (NonPlum; $\gamma_* = 1$); the DM halo can be cusped (Cusp; $\gamma_D = 1$) or cored (Core; $\gamma_D = 0$); and the (anisotropy) can be isotropic (Iso; $\beta = 0$), of generalized Osipkov–Merritt form (OM; Osipkov 1979; Merritt 1985; see equation 4), or tangentially anisotropic (Tan; $\beta = -0.5$).

Label	$[r_*, \alpha_*, \beta_*, \gamma_*]$	$[\rho_0, r_D, \alpha_D, \beta_D, \gamma_D]$	$\beta_0, \beta_\infty, n, r_a$	$R_{1/2}$
PlumCuspIso	[0.25, 2, 5, 0.1]	[6.4, 1, 1, 3, 1]	[0, 0, 1, 0]	0.25
PlumCoreIso	[1, 2, 5, 0.1]	[40, 1, 1, 3, 0]	[0, 0, 1, 0]	1.0
NonPlumCuspIso	[0.25, 2, 5, 1]	[6.4, 1, 1, 3, 1]	[0, 0, 1, 0]	0.20
NonPlumCoreIso	[1, 2, 5, 0.1]	[40, 1, 1, 3, 0]	[0, 0, 1, 0]	0.79
PlumCuspOM	[0.1, 2, 5, 0.1]	[6.4, 1, 1, 3, 1]	[0, 1, 2, 0.10]	0.1
PlumCoreOM	[0.25, 2, 5, 0.1]	[40, 1, 1, 3, 0]	[0, 1, 2, 0.25]	0.25
NonPlumCuspOM	[0.1, 2, 5, 1]	[6.4, 1, 1, 3, 1]	[0, 1, 2, 0.10]	0.079
NonPlumCoreOM	[0.25, 2, 5, 1]	[40, 1, 1, 3, 0]	[0, 1, 2, 0.25]	0.20
PlumCuspTan	[0.5, 0.5, 5, 0.1]	[2.39, 2, 1, 4, 1]	[-0.5, -0.5, 2, 0]	0.86
PlumCoreTan	[1.75, 0.5, 5, 0.1]	[3.0, 4.0, 1, 4, 0]	[-0.5, -0.5, 2, 0]	3.0
NonPlumCuspTan	[0.5, 0.5, 5, 1.0]	[2.39, 2, 1, 4, 1]	[-0.5, -0.5, 2, 0]	0.41
NonPlumCoreTan	[1.75, 0.5, 5, 1.0]	[3.0, 4.0, 1, 4, 0]	[-0.5, -0.5, 2, 0]	1.43

Osipkov–Merritt form (OM; see the next section), or tangentially anisotropic (Tan).

The isotropic and radially anisotropic spherical mocks are a subset of the mocks presented in Walker & Peñarrubia (2011) (see Section 2.1); the tangentially anisotropic mocks were generated using the method outlined in Dehnen (2009) (see Section 2.2). In all cases, we assume a double-power-law profile (Zhao 1996) for both the tracer distribution and the host DM halo:

$$\rho_X(r) = \rho_0 \left(\frac{r}{r_X} \right)^{-\gamma_X} \left[1 + \left(\frac{r}{r_X} \right)^{\alpha_X} \right]^{(\gamma_X - \beta_X)/\alpha_X}, \quad (3)$$

where ρ_0 is a normalization parameter, r_X sets the scale length, γ_X is the inner asymptotic logarithmic slope, β_X is the outer asymptotic logarithmic slope, and α_X controls the sharpness of the transition at r_X . For the tracers, we use the following notation: $\nu = \rho_*(r; \nu_0, r_*, \alpha_*, \beta_*, \gamma_*)$; for the DM, we write similarly: $\rho_D = \rho_D(r; \rho_0, r_D, \alpha_D, \beta_D, \gamma_D)$.

2.1 Radially anisotropic mocks

The velocity anisotropy coefficient (1) is assumed to depend on radius as follows:

$$\beta(r) = \frac{\beta_\infty r^n + \beta_0 r_a^n}{r^n + r_a^n}, \quad (4)$$

where β_0 is the asymptotic anisotropy at small radii, β_∞ is the asymptotic anisotropy at large radii, r_a is the transition radius, and n controls the sharpness of the transition. A familiar special case is the OM anisotropy profile (Osipkov 1979; Merritt 1985), used already above for the mock data, in which $\beta_0 = 0$, $\beta_\infty = 1$, and $n = 2$.

For the radially anisotropic mocks, the tracers are set up in equilibrium inside their host DM halo assuming an OM DF, as in Walker & Peñarrubia (2011).

2.2 Tangentially anisotropic mocks

The tangentially anisotropic mocks are set up using the ‘made to measure’ code from Dehnen (2009) that is an evolution of the method described in Syer & Tremaine (1996). In such methods, an N -body system is evolved for some time under its own self-gravity, adjusting

the masses of each particle so as to move towards a target phase-space distribution. The tangentially anisotropic mocks also assume the form given in equation (3) for the tracer and DM density profiles.

Tangential anisotropy is not expected theoretically, unless significant angular momentum is imparted to the system through mergers, or the system is orbiting within a strong tidal field³ (e.g. Read et al. 2006b). Given the lack of any strong theoretical motivation for a particular form of tangential anisotropy, we assume a constant $\beta = -0.5$ at all radii to explore whether tangential mocks can or cannot be successfully recovered.

3 METHODS

In this section, we briefly describe each of the four mass–orbit modelling methods that will be applied to the mock data.

3.1 GRAVSPHERE

GRAVSPHERE⁴ is described and tested in detail in Read & Steger (2017), Read et al. (2018), and Genina et al. (2020). It fits the LOS velocity variance, which can be written by combining the Jeans equation (2) with an equation projecting the velocities along the LOS, yielding (Binney & Mamon 1982)

$$\frac{\Sigma(R) \sigma_{\text{LOS}}^2(R)}{2} = \int_R^\infty \left(1 - \beta \frac{R^2}{r^2} \right) \nu \sigma_r^2 \frac{r \, dr}{\sqrt{r^2 - R^2}}, \quad (5)$$

where $\Sigma(R)$ denotes the tracer surface mass density at projected radius R .

The radial velocity variance is given by (van der Marel 1994, in this form by Mamon & Łokas 2005)

$$\sigma_r^2(r) = \frac{1}{\nu(r)g(r)} \int_r^\infty \frac{GM(\tilde{r})\nu(\tilde{r})}{\tilde{r}^2} g(\tilde{r}) d\tilde{r}, \quad (6)$$

³Note that in the case of strong tides, such tangential anisotropy would indicate a departure from the steady-state pseudo-equilibrium assumed by all of the methods explored here.

⁴A public version of the code PYGRAVSPHERE can be downloaded from <https://github.com/AnnaGenina/pyGravSphere>.

where

$$g(r) = \exp\left(2 \int_0^r \frac{\beta(\tilde{r})}{\tilde{r}} d\tilde{r}\right) \quad (7)$$

and $M(r)$ is the cumulative mass of the stellar system (due to all stars, gas, DM, etc.).

GRAVSPHERE uses a free-form, i.e. non-parametric, model for $M(r)$ that comprises a contribution from all visible matter and a contribution from ‘DM’ that is described by a sequence of power laws defined on a set of radial bins. By default, these bins are defined at $R = [0.25, 0.5, 1, 2, 4] R_{1/2}$, where $R_{1/2}$ is the projected half-light radius of the tracer stars. (This can be changed if the data quality warrant it, but in this paper we will use only this default choice.) The tracer light profile is also non-parametric, using a series sum of Plummer spheres, as in Rojas-Niño et al. (2016). This has the advantage that the mapping between the spherically averaged tracer density, $\nu(r)$, and the projected light profile, Σ_* , is analytic (Read & Steger 2017). Finally, the velocity anisotropy, $\beta(r)$, is assumed to have a form (4) that ensures broad generality while making the function $g(r)$ (equation 7) analytic. For assigning priors on the parameters in equation (4), we transform $\beta(r)$ to a symmetrized velocity anisotropy, as in Read et al. (2006a) and Read & Steger (2017):

$$\tilde{\beta} = \frac{\sigma_r^2 - \sigma_t^2}{\sigma_r^2 + \sigma_t^2} = \frac{\beta}{2 - \beta}. \quad (8)$$

This is bounded on $-1 < \tilde{\beta} < 1$ ($\tilde{\beta} = -1$ corresponds to full tangential anisotropy, $\tilde{\beta} = 1$ to full radial anisotropy, and $\tilde{\beta} = 0$ to isotropy), unlike β that tends to $-\infty$ for full tangential anisotropy.

GRAVSPHERE can also use split population or proper motion data, where available. By default, it also fits the two higher order ‘virial shape parameters’ (VSPs; Merrifield & Kent 1990; Richardson & Fairbairn 2014)

$$v_{s1} = \frac{2}{5} \int_0^\infty GM(5 - 2\beta) \nu \sigma_r^2 r dr \quad (9)$$

$$= \int_0^\infty \Sigma \langle v_{\text{LOS}}^4 \rangle R dR \quad (10)$$

and

$$v_{s2} = \frac{4}{35} \int_0^\infty GM(7 - 6\beta) \nu \sigma_r^2 r^3 dr \quad (11)$$

$$= \int_0^\infty \Sigma \langle v_{\text{LOS}}^4 \rangle R^3 dR. \quad (12)$$

The key advantage of these VSPs is that they involve fourth-order moments of the LOS velocities $\langle v_{\text{LOS}}^4 \rangle$, but depend only on $\beta(r)$ and not on its fourth-order counterparts (Merrifield & Kent 1990; Richardson & Fairbairn 2014; Read & Steger 2017). Thus, v_{s1} and v_{s2} allow us to obtain additional constraints on $\beta(r)$ via the LOS velocities, alleviating the mass–anisotropy degeneracy between the spherically averaged density profile $\rho(r)$ and the velocity anisotropy $\beta(r)$.

The errors on σ_{LOS} , $\langle v_{\text{LOS}}^4 \rangle$, v_{s1} , and v_{s2} are estimated as in Read et al. (2018), using a Monte Carlo method that incorporates the individual measurement errors on each star.

Finally, if proper motion data are available, GRAVSPHERE can also fit for the radial and tangential plane-of-sky velocity dispersions, σ_{POSr} and σ_{POST} , satisfying (e.g. Strigari et al. 2007; van der Marel & Anderson 2010; Read & Steger 2017)

$$\frac{\Sigma(R) \sigma_{\text{POSr}}^2(R)}{2} = \int_R^\infty \left(1 - \beta + \beta \frac{R^2}{r^2}\right) \frac{\nu(r) \sigma_r^2 r dr}{\sqrt{r^2 - R^2}}, \quad (13)$$

$$\frac{\Sigma(R) \sigma_{\text{POST}}^2(R)}{2} = \int_R^\infty (1 - \beta) \frac{\nu(r) \sigma_r^2 r dr}{\sqrt{r^2 - R^2}}. \quad (14)$$

This provides an alternative route to breaking the mass–anisotropy degeneracy since equations (5), (13), and (14) each has different dependences on β (see Read & Steger 2017, for further details).

GRAVSPHERE fits the above model to the surface density profile of tracer stars, $\Sigma_*(R)$, their LOS projected velocity-dispersion profile $\sigma_{\text{LOS}}(R)$, and their VSPs using the EMCEE affine invariant Markov chain Monte Carlo (MCMC) sampler from Foreman-Mackey et al. (2013). We assume uncorrelated Gaussian errors such that the Likelihood function is given by $\mathcal{L} = \exp(-\chi^2/2)$. We use as default 1000 walkers, each generating 5000 models and we throw out the first half of these as a conservative ‘burn in’ criterion. Please see Read & Steger (2017) for further details of our likelihood function, methodology, and priors.

3.2 DISCRETEJAM

The DISCRETEJAM method uses an alternative approach to solve the Jeans equations, which were laid out in Section 3.1. There are three key features of this method: (1) Both the tracer number density profile $\nu(r)$ and the underlying mass density profile $\rho(r)$ are parametrized in the form of multi-Gaussian expansions (MGEs; Emsellem, Monnet & Bacon 1994); (2) we fit to the discrete position measurements for each star, not to a binned tracer-density profile; and (3) we fit to the discrete velocity measurements for each star, not to a binned velocity-dispersion profile.

We model the dwarf galaxies using the Jeans Anisotropic MGE (JAM) models (Cappellari 2008; Watkins et al. 2013; Cappellari 2015). For the spherical mocks that are the focus of this paper, we use the spherical JAM models, which assume spherical symmetry and allow for anisotropy (defined in spherical coordinates) but do not include rotation.

An MGE is characterized by a set of Gaussian components, each with a width and a weight. If the tracer distribution is made up of N_t components where each component j has a weight v_j and a width s_j , then the tracer-density profile of the MGE is

$$\nu(r) = \sum_{j=1}^{N_t} v_j \exp\left(-\frac{r^2}{2s_j}\right). \quad (15)$$

Similarly, the mass density $\rho(r)$ can be parametrized by a set of N_m Gaussians with each component k having weight ρ_k and width s_k . The density profiles can be fitted analytically (where we fit MGEs to assumed functional forms and fit for the parameters of the functional forms) or non-parametrically (where we fit the MGE properties directly). Here, we choose an analytical approach, but see Hénault-Brunet et al. (2019) for a non-parametric methodology.

We assume that both the tracer density and DM density are described by equation (3). The models are insensitive to the normalization of the tracer density ν_0 , so this leaves us with four free parameters relating to the tracer distribution (r_* , α_* , β_* , and γ_*) and five relating to the DM distribution (ρ_0 , r_D , α_D , β_D , and γ_D). We assume that the anisotropy profile is of the generalized OM form (equation 4) with fixed $n = 2$. As in the GRAVSPHERE method, we symmetrize β_0 and β_∞ using equation (8) to avoid the high antisymmetry and infinite lower bound for β . This leaves three free components for the anisotropy: (r_a , $\tilde{\beta}_0$, and $\tilde{\beta}_\infty$).

We sample scale density ρ_0 and scale radii r_* , r_D , and r_a in log space as negative values would be unphysical; these parameters have

Table 2. Assumptions and parameters of different methods.

Method	GRAVSPHERE	DISCRETEJAM	MAMPOST	AGAMA	
Basis	Binned v_{LOS} + VSPs	Gaussian v_{LOS}	Gaussian $v_{3\text{D}}$	$f(E, L)$	$f(J_r, L)$
Radial binning	Yes	No	No	No	
$\rho_{\text{D}}(r)$	Five-piece power law	MGE fit to equation (3)	Equation (3), $\alpha = 1$	Equation (3)	
$v_*(r)$	Sum of Plummer models	MGE fit to equation (3)	Equation (3), $\alpha = 2, \beta = 5$	Equation (3)	Fitted by DF
$\beta_*(r)$	Equation (4)	Equation (4), $n = 2$	Equation (4), $n = 2$	Equation (4), $n = 2, \beta_\infty = 1$	Fitted by DF
# of free parameters	17	12	9	11	11
Ranges of free parameters:					
$\log_{10}(M_{200c}/M_\odot)$	Unbounded	Unbounded	True ± 1	Unbounded	
r_{D}/kpc	–	$0.25 r_* \leftrightarrow 50 r_*$	True ± 0.5 dex	$0.1 \leftrightarrow 100$	
α_{D}	–	$0.5 \leftrightarrow 2.5$	1	$0.5 \leftrightarrow 2.5$	
β_{D}	–	$2 \leftrightarrow 5$	$2 \leftrightarrow 6$	$2.2 \leftrightarrow 6$	
γ_{D}	–	$-0.5 \leftrightarrow \beta_{\text{D}}$	$-0.1 \leftrightarrow 2$	$-0.5 \leftrightarrow 1.9$	
$\log_{10}(r_*/\text{kpc})$	–	$-2 \leftrightarrow 1$	True ± 0.3	$-2 \leftrightarrow 1$	–
α_*	–	$0.5 \leftrightarrow 2.5$	2	$0.5 \leftrightarrow 3$	–
β_*	–	$2 \leftrightarrow 7$	5	$3.5 \leftrightarrow 6$	–
γ_*	–	$-0.5 \leftrightarrow \beta_*$	$-0.05 \leftrightarrow 1.5$	$0 \leftrightarrow 1.9$	–
$\tilde{\beta}_0$	$-1 \leftrightarrow 1$	$-0.95 \leftrightarrow 1$	$-0.9 \leftrightarrow 1$	$-0.5 \leftrightarrow 1$	–
$\tilde{\beta}_\infty$	$-1 \leftrightarrow 1$	$-0.95 \leftrightarrow 1$	$-0.9 \leftrightarrow 1$	1	–
$\log_{10}(r_a/\text{kpc})$	$-2 \leftrightarrow 0$	$\log_{10}(r_*) \pm 0.3$	True ± 0.3	$-2 \leftrightarrow 5$	–
n	$1 \leftrightarrow 10$	2	2	2	–
Γ	–	–	–	–	$0 \leftrightarrow 2.8$
B	–	–	–	–	$3.2 \leftrightarrow 12$
Minimization	EMCEE	EMCEE	COSMOMC	EMCEE	
# of chains	1000	100	6	32	
Length of chains	5000	20 000	90 000	$\text{few} \times 10^3$	
CPU minutes (10^3 tracers)	360	$\mathcal{O}(10^4)^a$	6×15 (the 6 in \parallel)	$\mathcal{O}(10^3)$	

Note. ^aThe run time speeds up if fewer Gaussians are used; a non-parametric approach would use many fewer Gaussians and could be significantly faster.

the potential to explore many orders of magnitude in size when model fitting, and a dimensionless parameter space is generally more efficient to search. The other parameters are already dimensionless by definition.

We use an unbounded flat prior on $\log \rho_0$. We restrict the range of the tracer scale radii to $-2 \leq \log_{10}(r_*/\text{kpc}) \leq 1$ and the DM scale radii to $0.25 \leq r_{\text{D}}/r_* \leq 50$, but otherwise assume flat priors within these ranges. For transition parameters α_* and α_{D} , we use a flat prior in $0.5 \leq (\alpha_*, \alpha_{\text{D}}) \leq 2.5$; this eliminates models that change too sharply or too slowly.

For the outer density slopes, we use flat priors in $2 \leq \beta_* \leq 7$ and $2 \leq \beta_{\text{D}} \leq 5$, where the upper limits restrict the steepness based on observed values. Models with $(\beta_*, \beta_{\text{D}}) \leq 3$ are unphysical as they are not finite; however, some mocks have outer slopes of 3, meaning that the correct answer is at the edge of the parameter space. To allow the fits to fully explore the parameter space, we use lower limits of 2 for the outer slopes.

For the inner density slopes, we use flat priors in $-0.5 \leq \gamma_* \leq \beta_*$ and $-0.5 \leq \gamma_{\text{D}} \leq \beta_{\text{D}}$, where the upper limits ensure that the inner slope is shallower than the outer slope. Formally, for a lower limit of 0 on the inner slopes we would be appropriate here; otherwise, we have a negative density component in the MGE fit. However, as above, some mocks have inner slopes of 0, thus at the edge of the parameter space. So to allow the models to fully explore the region of parameter space around the true value, we use lower limits of -0.5 on the inner slopes.

We assume a flat prior on the anisotropy scale radii in $0.5 \leq r_a/r_* \leq 2$; both the isotropic and tangential mocks have flat anisotropy profiles in which case the notion of an anisotropy transition radius becomes somewhat meaningless, with this choice of prior we give the models some flexibility, but avoid fitting a potentially undefined parameter. In theory, $-1 \leq \tilde{\beta} \leq 1$. In practice, we set a lower bound of $\beta = -40$, which corresponds to $\tilde{\beta} \sim -0.95$ as extremely

tangential models with $\tilde{\beta} \sim -1$ are computationally challenging (and physically unlikely). We use a flat prior on $\tilde{\beta}$ within these limits.

For a given set of density parameters, we calculate $\nu(r)/\nu_0$ or $\rho(r)$ using equation (3). To this, we fit an MGE using MGEFIT (Cappellari 2002), which we then deproject to obtain the projected surface mass and tracer-density profiles as needed for the JAM models.⁵ To each component j of the tracer MGE, we assign an anisotropy β_j by calculating the value of the generalized OM profile at the radius of each Gaussian component s_j .

Our observables are the spatial distribution of the tracer particles and the velocity measurements of the tracer particles. We fit to both discretely; that is we do not bin the tracers but consider each star individually. We follow the approach laid out in Watkins et al. (2013), modified as described below. This method is flexible and can be used to fit only LOS velocity information, only proper motions, or full 3D velocity information. The original method was designed to fit a binned surface brightness profile, whereas here we fit the tracer density discretely as well.

Consider a tracer particle i at a projected distance R_i from the centre of the dwarf with velocity $v_{X,i} \pm \delta_{X,i}$, where X can be the right ascension PM (α), the declination PM (δ), or the LOS (z), and the uncertainties $\delta_{X,i}$ are assumed to be Gaussian. To fit the spatial distribution of the tracers, we use the projected tracer density MGE to calculate the normalized probability $P_i = P(R_i)$ of observing a star at projected radius R_i . Then, the likelihood of all N tracer particles is

$$\mathcal{L}_* = \prod_{i=1}^N P_i. \quad (16)$$

⁵A PYTHON package MGETOOLS for manipulating MGEs is available at <http://www.github.com/lauralwatkins/mgetools>.

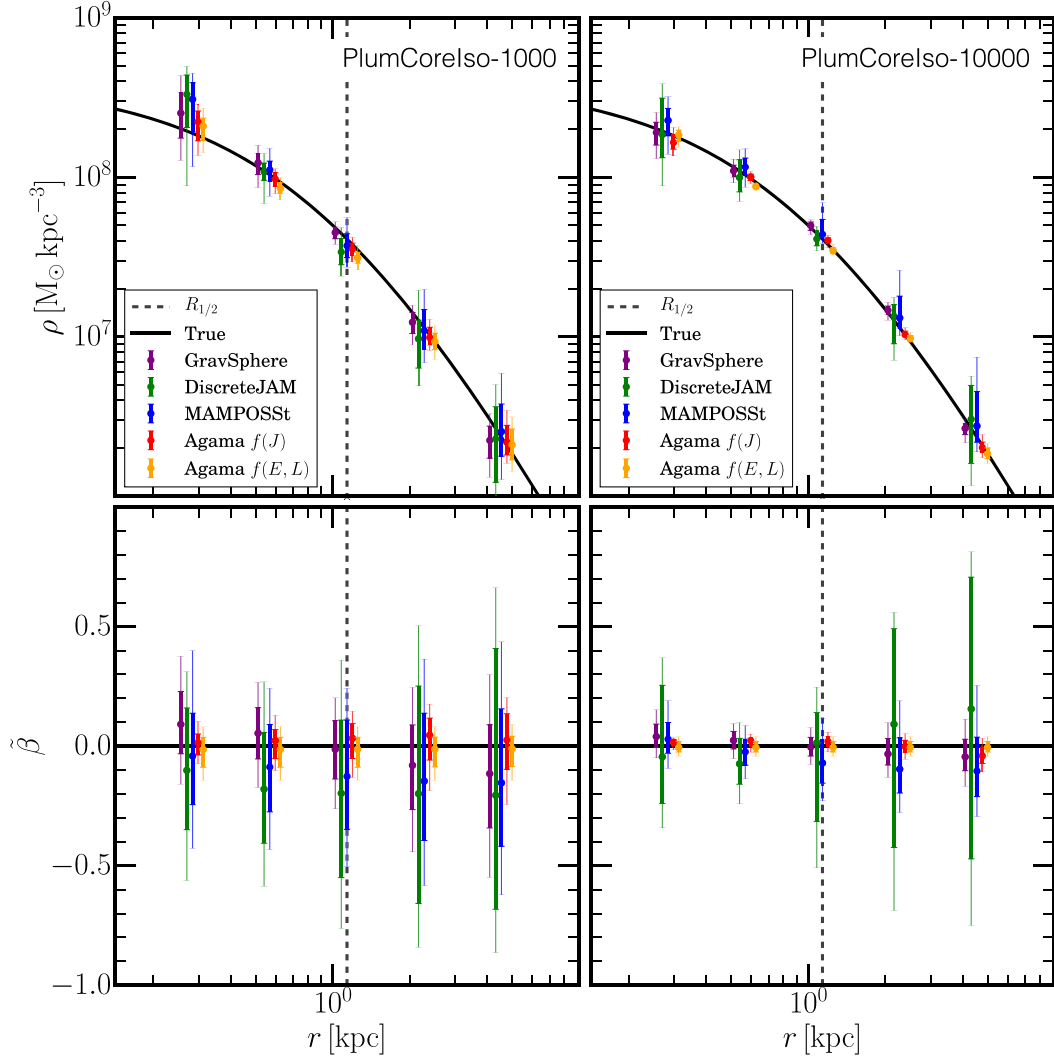


Figure 1. Recovery of the density (top) and symmetrized velocity anisotropy (bottom; see equation 8) for the PlumCoreIso mocks, with LOS velocities for 1000 (left) and 10 000 (right) tracer stars. The data points show the recovery at $R = [0.25, 0.5, 1, 2, 4] R_{1/2}$, where $R_{1/2}$ is the projected half-light radius (vertical dashed line). The thick/thin error bars mark the 68 per cent/95 per cent confidence intervals, respectively. The different colours show results for GRAVSPHERE (purple), DISCRETEJAM (green), MAMPOSST (blue), AGAMA $f(J)$ (red), and $f(E, L)$ (orange), as marked in the legend. Each of the methods is slightly offset left–right from one another to aid clarity (where points are offset, we show the density profile recovery at exactly this offset point). The true mock density and velocity anisotropy profiles are shown by the black lines.

To fit the velocity measurements, we assume that the LOS velocity distribution (LOSVD) at a given radius is Gaussian with a mean velocity of 0 (due to the assumptions of spherical symmetry and no rotation) and velocity dispersion $\sigma_{X,i}$, which we calculate from the JAM model. Then, the likelihood of all N measurements is

$$\mathcal{L}_{\text{kin},X} = \prod_{i=1}^N \frac{1}{\sqrt{2\pi (\delta_{X,i}^2 + \sigma_{X,i}^2)}} \exp\left(\frac{-v_{X,i}^2}{2(\delta_{X,i}^2 + \sigma_{X,i}^2)}\right), \quad (17)$$

which accounts for the fact that the observed dispersion is a convolution of the true dispersion $\sigma_{X,i}$ and the measurement uncertainties $\delta_{X,i}$. When using only LOS velocity information, the total likelihood \mathcal{L} for the spatial and kinematic distributions combined is then

$$\mathcal{L} = \mathcal{L}_* \mathcal{L}_{\text{kin},z}. \quad (18)$$

When using PM and LOS kinematic information, the total likelihood \mathcal{L} becomes

$$\mathcal{L} = \mathcal{L}_* \mathcal{L}_{\text{kin},\alpha} \mathcal{L}_{\text{kin},\delta} \mathcal{L}_{\text{kin},z}, \quad (19)$$

assuming that the measurements and uncertainties are not correlated.

The posterior probability of the model given the data is then obtained by multiplying together the likelihood and parameter priors. By maximizing the posterior, we can locate the family of models that best fit the data. To efficiently explore our parameter space and locate the high-posterior region, we use EMCEE (Foreman-Mackey et al. 2013) with 100 walkers and for 20 000 steps.

3.3 MAMPOSST

MAMPOSST (Mamon et al. 2013) is similar to DISCRETEJAM, as it fits the full distribution of the individual tracers in projected phase

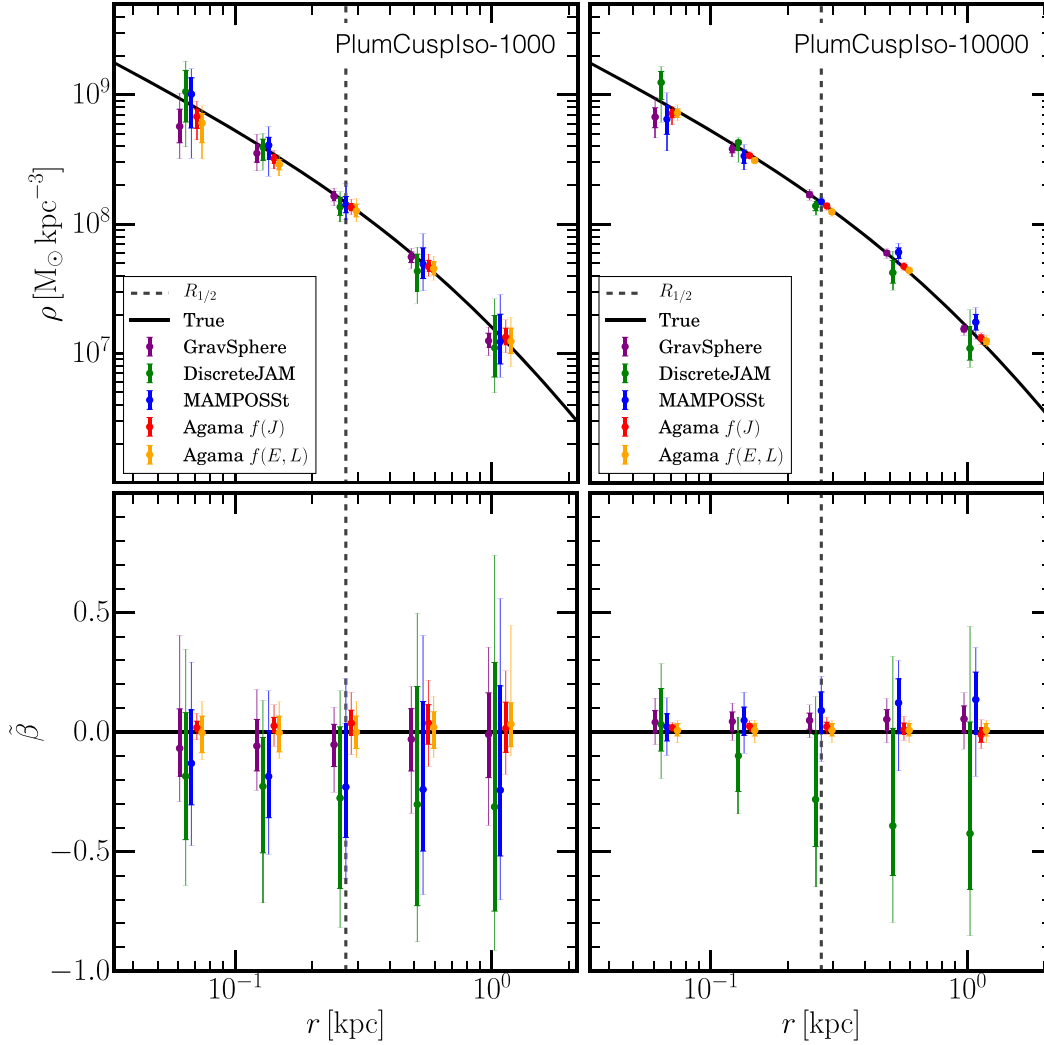


Figure 2. As Fig. 1, but for the PlumCuspIso mock.

space. However, while DISCRETEJAM assumes that the LOS velocities are Gaussian distributed, MAMPOSSt avoids this assumption, since anisotropy affects the shape of the LOSVD (Merritt 1987), and assumes instead that the local three-dimensional velocity distribution is Gaussian distributed. More precisely, MAMPOSSt assumes parametric forms for the mass, tracer density, and anisotropy profiles. In situations where only LOS velocities are available, the density of tracers in projected phase space (projected radius R and the LOS velocity v_{LOS}) is the integral of the local velocity distributions along the LOS:

$$g(R, v_{\text{LOS}}) = 2 \int_R^\infty h(v_{\text{LOS}} | R, r) v(r) \frac{r dr}{\sqrt{r^2 - R^2}}. \quad (20)$$

MAMPOSSt assumes that the *local* velocity DF h is a Gaussian of zero mean:

$$h(v_{\text{LOS}} | R, r) = \mathcal{G}(v_{\text{LOS}}, 0, \sigma_{\text{LOS}}^2), \quad (21)$$

where $\sigma_{\text{LOS}}^2(R, r) = [1 - \beta(r)R^2/r^2] \sigma_r^2$ as in the integrand of equation (5). The likelihood is given by

$$-\ln \mathcal{L} = - \sum_i \ln q(R_i, v_i | \theta), \quad (22)$$

where i are the indices of the individual tracers, v_i is the LOS velocity for tracer particle i , θ is the vector of parameters, and q is the probability density:

$$q(R, v) = \frac{2\pi R g(R, v)}{N_p(R_{\text{max}}) - N_p(R_{\text{min}})}, \quad (23)$$

where $N_p(R) = \int_0^R 2\pi R' \Sigma(R') dR'$ is the predicted number of tracers expected within the projected radius R .

MAMPOSSt has recently been generalized to include handling of proper motion data (MAMPOSSt-PM; Mamon & Vitral, in preparation). The full local velocity DF is assumed to be the product of three Gaussians:

$$\begin{aligned} h(v | R, r) = & \mathcal{G}(v_{\text{LOS}}, 0, \sigma_{\text{LOS}}^2(R, r)) \\ & \times \mathcal{G}(v_{\text{POSr}}, 0, \sigma_{\text{POSr}}^2(R, r)) \\ & \times \mathcal{G}(v_{\text{POST}}, 0, \sigma_{\text{POST}}^2(R, r)), \end{aligned} \quad (24)$$

where the plane-of-sky velocity variances are $\sigma_{\text{POSr}}^2(R, r) = [1 - \beta(r) + \beta(r)R^2/r^2] \sigma_r^2(r)$ and $\sigma_{\text{POST}}^2(R, r) = [1 - \beta(r)] \sigma_r^2(r)$ as given in the integrands of equations (13) and (14), respectively, where

σ_r^2 is the solution of the Jeans equation taken from equations (6) and (7).

The likelihood is now given by

$$-\ln \mathcal{L} = - \sum_i \ln q(R_i, v_i | \boldsymbol{\theta}), \quad (25)$$

where i are the indices of the individual tracers, \mathbf{v}_i is the velocity vector for tracer particle i , and $\boldsymbol{\theta}$ is the vector of parameters, while the probability density q is now

$$q(R, v) = \frac{2\pi R g(R, v)}{N_p (R_{\max}) - N_p (R_{\min})}. \quad (26)$$

For both MAMPOSST and MAMPOSST-PM, measurement uncertainties are added in quadrature to the predicted LOS and plane-of-sky velocity dispersions in the local velocity DF h .

The mass profile is assumed to follow equation (3), for which the enclosed total mass (here assuming only DM contributes) is

$$M(r) = \frac{4\pi}{3-\gamma} \rho_0 r^3 \left(\frac{r_D}{r}\right)^\gamma \times {}_2F_1 \left[\frac{3-\gamma}{\alpha}, \frac{\beta-\gamma}{\alpha}, \frac{3-\gamma}{\alpha} + 1, - \left(\frac{r}{r_D}\right)^\alpha \right], \quad (27)$$

where $\alpha = \alpha_D$, $\beta = \beta_D$, $\gamma = \gamma_D$, and ${}_2F_1$ is the ordinary hypergeometric function. The MAMPOSST analyses assume $\alpha_D = 1$ and free inner and outer slopes. The tracer-density profile is also described by equation (3), with $\beta_* = 5$, $\alpha_* = 2$, and a free inner slope γ_* . Finally, the velocity anisotropy profile has the form of equation (4) with $n = 2$ and free β_0 , β_∞ , and r_a .

The nine free parameters are thus the mass normalization, the mass scale radius r_2 , the DM inner and outer slopes γ_D and β_D , the stellar scale radius r_* and inner density slope γ_* , the inner and outer anisotropies β_0 and β_∞ , and the anisotropy radius r_a .

The minimization is performed with the COSMOMC (Lewis & Bridle 2002) MCMC sampler, using 6 chains with 90 000 elements, discarding the first 15 000 elements of each chain for the analysis. We adopted $R_{\min} = 0$ and $R_{\max} = 1.9$ kpc for our allowed range of projected radii. Flat priors were used on the log masses, log scales, and on the indices and symmetrized anisotropies, with ranges listed in Table 2.

3.4 DF fitting with the AGAMA library

The AGAMA library (Vasiliev 2019) is a C++ library for constructing galaxy models using DFs. A DF, $f(\mathbf{w})$, fully describes the distribution of a population of stars with phase-space coordinates, $\mathbf{w} \equiv \{\mathbf{x}, \mathbf{v}\}$. In a steady state, f only depends on the integrals of motion, $\mathbf{I}(\mathbf{w})$, supported by the potential. The log likelihood of a model \mathcal{M} characterized by the potential $\Phi(r)$ and the DF $f(\mathbf{I})$ is given by the sum of log probabilities of each star being drawn from this DF (if we assume that all stars could be observed; i.e. the selection function is unity):

$$\ln \mathcal{L} = \sum_{i=1}^{N_{\text{stars}}} \ln f[\mathbf{I}(\mathbf{w}_i; \Phi)]. \quad (28)$$

In the case of incomplete data, we need to marginalize over the probability of each star by integrating over missing phase-space coordinates. In the case of errors, we need to convolve with the distribution of errors. For instance, if we have only the projected radius R and the LOS velocity v_z that carries a Gaussian error δv_z ,

the above expression is modified to

$$\ln \mathcal{L} = \sum_{i=1}^{N_{\text{stars}}} \ln \left\{ \int_{-\infty}^{\infty} dz \int_{-\infty}^{\infty} dv_x \int_{-\infty}^{\infty} dv_y \int_0^1 d\xi \times f \left[\mathbf{I}(R, z, v_x, v_y, v_z + \sqrt{2} \delta v_z \text{erf}^{-1}(2\xi - 1); \Phi) \right] \right\}, \quad (29)$$

where $\xi \sim \mathcal{U}(0, 1)$ marginalizes over velocity error.

We evaluate these multidimensional integrals by using the Monte Carlo approach. For each star with index i , we construct an array of $N_{\text{samp}} \gtrsim 10^3$ ‘sample points’ with missing phase-space coordinates $\mathbf{w}_{i,k}$ assigned from a suitable prior distribution $P_i(\mathbf{w})$. The marginalized value of DF for the i -th star is $f_i = \sum_{k=1}^{N_{\text{samp}}} f[\mathbf{I}(\mathbf{w}_{i,k}; \Phi)] / P_i(\mathbf{w}_{i,k})$. Some of these samples would have a zero probability (e.g. if the energy is positive), but as long as there remain samples in a valid region of phase space, the total probability is positive, and hence the log likelihood is finite.

To eliminate the impact of Poisson noise on the relative odds of different models, we use the same set of sample points for all models (e.g. McMillan & Binney 2013), and to further improve the accuracy, we design the priors according to the importance sampling approach; i.e. we place samples more densely in regions that are expected to have a higher value of f , thereby approximately equalizing their contribution to the total sum. Namely, to sample the missing z coordinate, we determine a smooth non-parametric estimate of the surface density profile of tracers, deproject it to obtain an estimate of the 3D density $\rho(r)$, and sample z from $\rho(\sqrt{R^2 + z^2})$ at the position of each star R_i . For the missing velocity components, we estimate the velocity dispersion of the entire system from the measured values $v_{z,i}$, and sample $v_{x,y}$ from a heavy-tailed bell-like distribution with the same dispersion. The non-uniform sampling is accounted for when computing the contribution P_i of each sample point to the marginalization integral; the estimates of the density profile and velocity dispersion are only used during the initial resampling step, but not in subsequent fitting.

In a spherical system, the integrals of motion are the energy E and angular momentum L per unit mass. Alternatively, one may use actions as the integrals of motion; in this case, E is replaced with the radial action J_r , defined as

$$J_r \equiv \frac{1}{\pi} \int_{r_{\min}}^{r_{\max}} v_r dr = \frac{1}{\pi} \int_{r_{\min}}^{r_{\max}} dr \sqrt{2[E - \Phi(r)] - L^2/r^2}, \quad (30)$$

where r_{\min} and r_{\max} are the roots of the expression under the radical. For each choice of potential, we pre-compute a high-accuracy 2D interpolating spline for efficient evaluation of $J_r(E, L)$; thus, using the action variables adds a minor overhead compared to the use of just the classical integrals E and L . The advantages of action variables are not apparent in the context of spherical models, but are more important in non-spherical cases.

For the density profile of the DM, responsible for the gravitational potential, we adopt the same five-parameter model in equation (3) that was used to produce the mocks. On the other hand, we use two different families of DF: One is expressed in terms of E and L and the other in terms of radial action J_r and the sum of two other actions $L \equiv J_z + |J_\phi|$; both have six free parameters.

The first DF family is constructed from a given tracer-density profile, using the Cuddeford–Osipkov–Merritt inversion formula

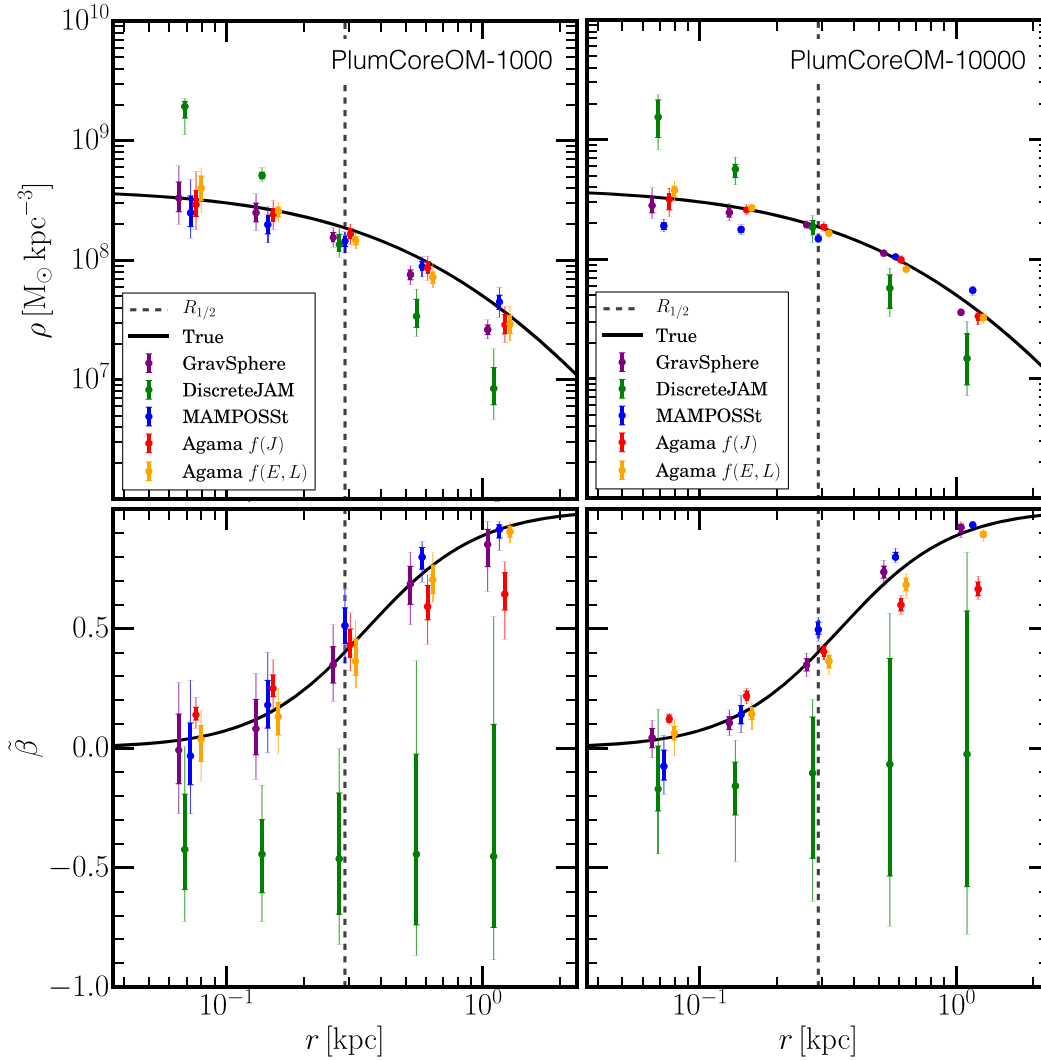


Figure 3. As Fig. 1, but for the PlumCoreOM mock.

(Cuddeford 1991). In this case, we use equation (3) for the tracer-density profile, which has four free parameters: α_* , β_* , γ_* , and r_* (the fifth one, ν_0 , is fixed by the normalization constraint). Two other parameters β_0 and r_a define the anisotropy profile (equation 4 with $n = 2$ and $\beta_\infty = 1$). This DF family includes the true DF of all variants of models, so we expect to be able to recover the true parameters, given enough data.

The second family is a generalization of the action-based DF presented in Posti et al. (2015):

$$f(J_r, L) = A \frac{\left(1 + [J_0/\{pJ_r + (1-p)L\}]^\eta\right)^{\Gamma/\eta}}{\left(1 + [\{qJ_r + (1-q)L\}/J_0]^\eta\right)^{(B-\Gamma)/\eta}}. \quad (31)$$

Here, the power-law indices Γ and B control the steepness of the density profile at small and large radii, correspondingly; J_0 determines the transition between the two asymptotic regimes, η controls the sharpness of this transition, the mixing parameters p and q are responsible for the velocity anisotropy at small and large radii, and finally A is the overall normalization constant, which ensures that the integral of f over the entire phase space is unity (it is computed numerically for each choice of six DF parameters and is not a free

parameter by itself). In this case, there are no separate parameters for the density profile, because it is determined from the DF and the potential: $\nu(r) = \iiint d^3\mathbf{v} f[\mathbf{I}(\mathbf{x}, \mathbf{v}; \Phi)]$. However, we do not need the density per se, since we fit the joint DF of position and velocity. Since the true DF used to generate the mock data does not belong to this family of models, we may expect that best-fitting parameters of the potential could be biased by the constrained form of the adopted DF.

To explore the parameter space, we use the EMCEE code with 32 walkers evolved for several thousand steps. The evaluation of model likelihoods is performed using AGAMA.⁶

3.5 Summary of methods and assumptions

Table 2 summarizes the different assumptions and parametrizations of the different methods.

⁶The AGAMA library, together with the complete PYTHON program performing the DF fitting for this study, is available at <http://agama.software>.

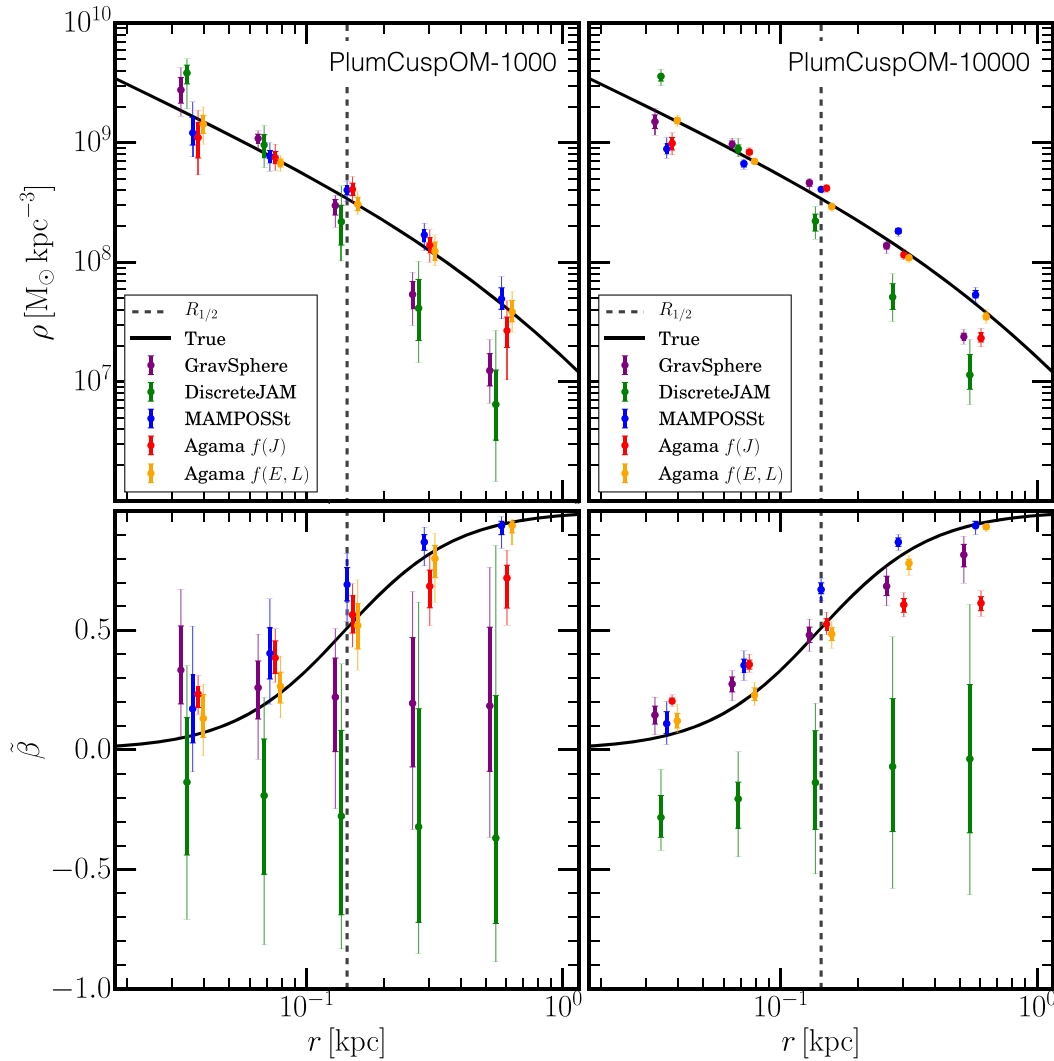


Figure 4. As Fig. 1, but for the PlumCuspOM mock.

4 RESULTS

In this section, we present results for each method described in Section 3 for the recovery of the total density and stellar velocity anisotropy at $R = [0.25, 0.5, 1, 2, 4]R_{1/2}$, where $R_{1/2}$ is the projected half-light radius, using only LOS velocity data for 1000 and 10 000 tracers. For brevity, we focus on the ‘Plum’ mocks that are representative of the results from the full suite; for completeness, we present results for the ‘NonPlum’ mocks in Appendix A. For all mocks, we applied 2 km s^{-1} velocity errors to be consistent with current spectroscopic accuracy for dwarf galaxy data (see Section 1).

4.1 Isotropic mocks

Figs 1 and 2 show the recovery of the density (top) and *symmetrized velocity anisotropy* (bottom; see equation 8) for the isotropic mocks for 1000 (left) and 10 000 (right) tracers. For these isotropic mocks, all four methods perform similarly well, with the results improving with increased sampling. The density profile is already well recovered with 1000 tracers, with all methods recovering the input solution within their 95 per cent confidence intervals over the radial range $0.25 < R/R_{1/2} < 4$.

However, the uncertainty on $\tilde{\beta}$ remains substantial for 1000 tracers. Increasing their number to 10 000, AGAMA and GRAVSPHERE obtain the tightest constraints on $\tilde{\beta}$, with AGAMA – which uses the full shape information in the DF – having the smallest uncertainties.

4.2 Radially anisotropic mocks

Moving to radially anisotropic mocks (Figs 3 and 4), we now see a larger difference between the different methods. Each method recovers some parts of the solution better than others, highlighting the value of modelling the data with multiple techniques. Overall, the accuracy of recovery of the potential is tightly linked to the ability of the method to recover the anisotropy profile of the tracers (cf. Read & Steger 2017).

For 1000 tracers, MAMPOSST and AGAMA $f(E, L)$ recover $\tilde{\beta}(r)$ and $\rho(r)$ over the radial range $0.25 < R/R_{1/2} < 4$ within their 95 per cent confidence intervals, for both the PlumCoreOM and PlumCuspOM mocks. This may reflect the fact that in these methods, the assumed functional forms for the mass, light, and $\tilde{\beta}$ profiles encompass the true solution [in particular, $\beta_\infty = 1$ in the AGAMA $f(E, L)$ models]. By contrast, the AGAMA $f(J)$ models do not fully

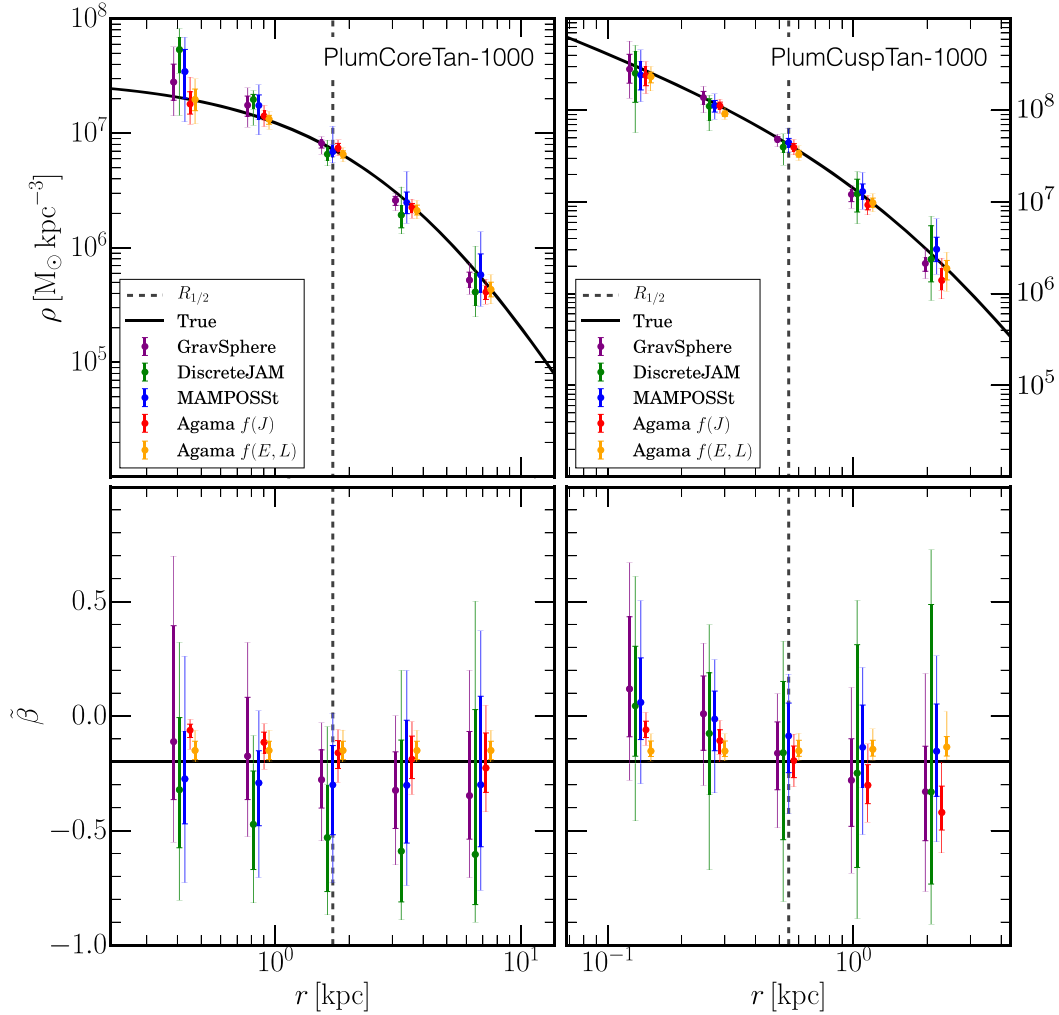


Figure 5. As Fig. 1, but for mocks PlumCoreTan (left) and PlumCuspTan (right) with 1000 tracer stars.

recover the $\tilde{\beta}$ profile, being more radially anisotropic at small r and less radially anisotropic at large r . This negatively impacts the accuracy of potential recovery in the PlumCuspOM case, although not in the PlumCoreOM case. GRAVSPHERE recovers the anisotropy profile within its 95 per cent confidence intervals in the PlumCoreOM case, but performs more poorly in the PlumCuspOM case. Both DISCRETEJAM and GRAVSPHERE are biased to low $\rho(r)$ beyond $R_{1/2}$, while DISCRETEJAM is also biased to high $\rho(r)$ inside $R_{1/2}$ for the PlumCoreOM mock. This owes to a bias towards tangential anisotropy for the DISCRETEJAM method in both PlumCoreOM and PlumCuspOM mocks that does not diminish even for 10 000 tracer stars. This behaviour is also seen in the GRAVSPHERE code if the VSPs are not used in the fit. Read & Steger (2017) show that this bias owes to the mass–anisotropy degeneracy, combined with the true solution for this mock lying on the edge of the hypervolume of acceptable models. Indeed, they show that the correct model is recovered within the full MCMC chains, but is rare as compared to the large number of tangentially anisotropic models that fit the data similarly well.

Finally, moving to 10 000 tracers, bias starts to creep in or becomes more statistically significant in most of the methods. The AGAMA $f(E, L)$ models still produce good fits within their 95 per cent confidence intervals, while the $f(J)$ models retain the biases in the anisotropy profile in both cases, and in $\rho(r)$ in the PlumCuspOM

case, reflecting the fact that the assumed DF differs from the one used to set up the mocks (cf. the earlier discussion on this in Section 1). MAMPOSST also starts to show similarly biased behaviour, with the inner density underestimated at small radii for the PlumCuspOM and PlumCoreOM mocks, and bias now present in the recovery of $\tilde{\beta}(r)$. This likely owes to the assumed Gaussian form of the local DF being a good, but not perfect, approximation to its true shape. The DISCRETEJAM method – which is not able to break the mass–anisotropy degeneracy with LOS data alone – retains the bias seen in its recovery of the 1000 star mocks, but with smaller error bars. The GRAVSPHERE method – which is designed to make as few assumptions as possible about the form of the gravitational potential and the DF – approaches the true solution more closely, although some bias towards lower $\rho(r)$ remains at large radii for the PlumCuspOM mock. This bias is, however, significantly reduced as compared to the 1000 star solution.

Finally, we note that some of the differences in performance between the different methods owe also to their different priors (see Table 2). GRAVSPHERE has the loosest priors of all methods presented here and, correspondingly, the greatest challenge in recovering the mocks. By contrast, MAMPOSST assumes tighter priors that are symmetrized around the true solution, DISCRETEJAM uses priors for the anisotropy and DM scale radii that are tightly linked to the stellar

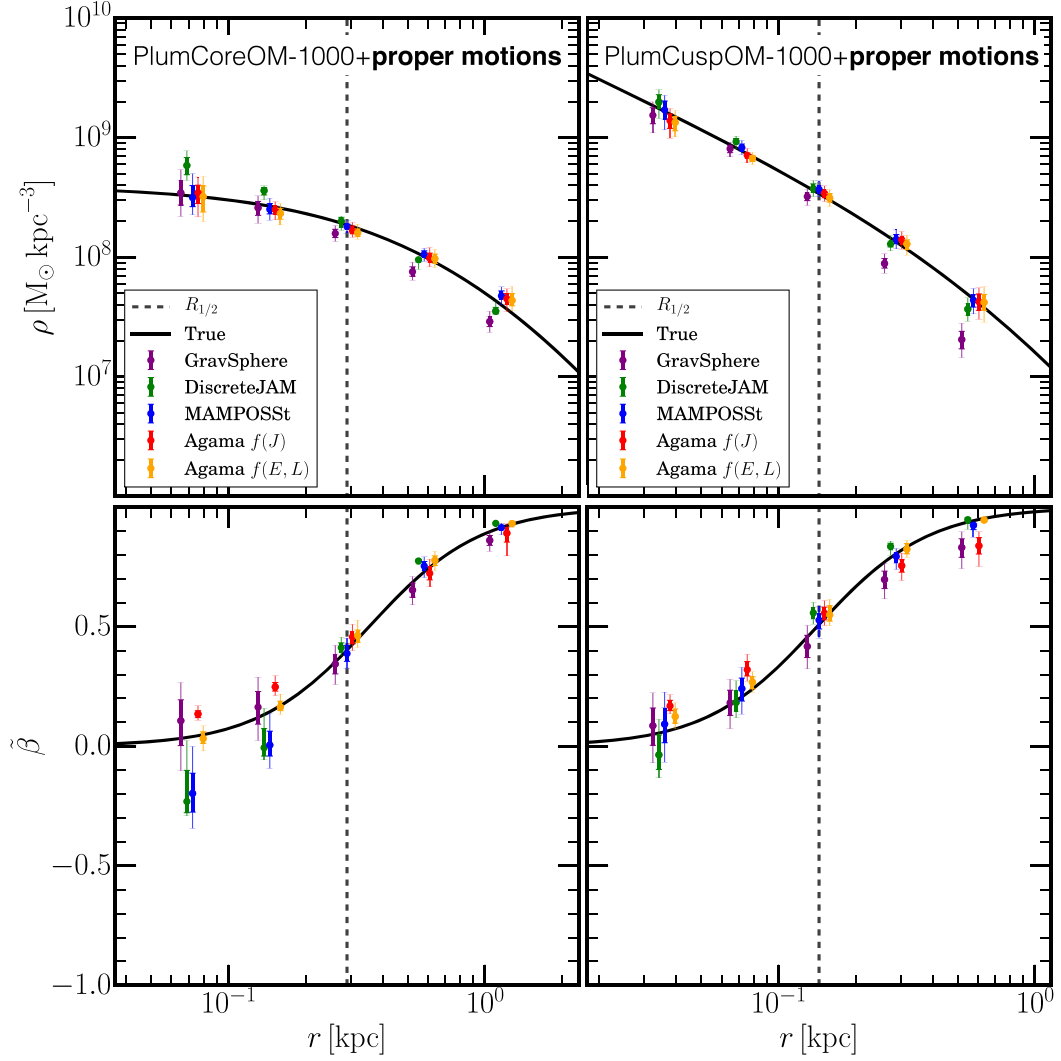


Figure 6. As Fig. 1, but for mocks PlumCoreOM (left) and PlumCuspOM (right) including also proper motion data (see the text for details).

density scale radius (which is itself very well recovered), and AGAMA $f(E, L)$ assumes $\beta_\infty = 1$, as in the mocks. Moreover, DISCRETEJAM, MAMPOSST, and AGAMA each assumes the same functional form for the mass profile as in the mock data (with MAMPOSST fixing the value of α_D), whereas GRAVSPHERE does not. As such, we cannot really speak of any one method being ‘superior’ to the others; rather, each has its strengths and weaknesses.

4.3 Tangentially anisotropic mocks

In Fig. 5, we show our results for the tangentially anisotropic mocks, PlumCoreTan and PlumCuspTan, assuming 1000 tracer stars. Notice that, similarly to the isotropic mocks, all methods recover $\rho(r)$ within their 95 per cent confidence intervals over the range $0.25 < R/R_{1/2} < 4$ (top panels), though for the PlumCoreTan mock, DISCRETEJAM is biased (at 68 per cent confidence) towards cuspy, tangentially anisotropic mocks and MAMPOSST marginally so. This is similar, though less severe, to the bias seen for the PlumCoreOm mock and owes to the mass–anisotropy degeneracy (see discussion above).

All methods successfully detect the tangential anisotropy, though for 1000 tracers, this is only statistically significant near the half-

light radius (vertical dashed line). Interestingly, both the AGAMA $f(E, L)$ and AGAMA $f(J)$ methods become biased at greater than their 95 per cent confidence intervals. AGAMA $f(J)$ is overly isotropic in the inner regions and, for PlumCuspTan, overly tangential in its outer regions, while AGAMA $f(E, L)$ is overly isotropic at all radii. These biases reflect the assumed parametrization of the DF and the choice of priors. As discussed above and in Section 1, this will lead to bias if the phase-space DF of the mock data is inconsistent with these assumptions, as is the case here. Indeed, the tangentially anisotropic mocks present a particular challenge for the AGAMA $f(E, L)$ models, since the true value of $\beta = -0.5$ lies at the boundary of the allowed range (for technical reasons, anisotropic DFs computed by the Cuddeford–Osipkov–Merritt method are restricted to have $\beta_0 \geq -0.5$).

4.4 Adding proper motion data

In Fig. 6, we show the performance of all methods when adding proper motion data. For this, we consider 1000 tracers for the PlumCuspOM and PlumCoreOM mocks assuming 2 km s^{-1} errors on all three components of the velocity (the other mock data produced

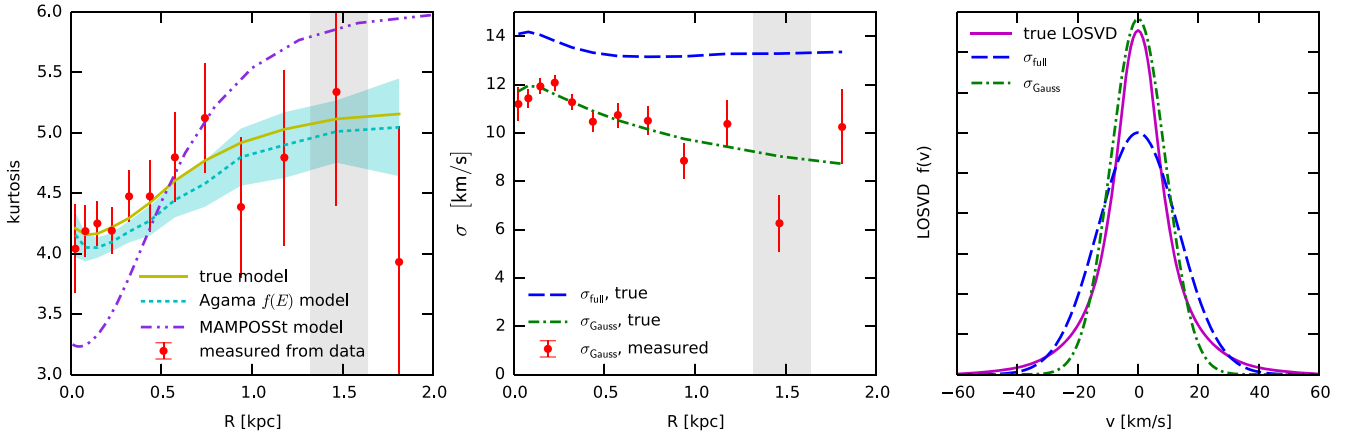


Figure 7. Illustration of non-Gaussianity of LOSVD in a radially anisotropic model (PlumCoreOM). Left-hand panel: radial profile of the LOS kurtosis $\kappa \equiv \overline{v^4}/\sigma_{\text{full}}^4$, where $\sigma_{\text{full}}^2 \equiv \overline{v^2}$ is the LOS velocity dispersion (full second moment of the velocity distribution). For a Gaussian LOSVD, $\kappa = 3$; a higher value indicates a fat-tailed distribution. Solid yellow line is the true κ in the given model; red points with error bars are the binned measured values in the 10^4 -star mock data set; dotted cyan line with a shaded region is the mean and the 68 per cent interval of values in the AGAMA $f(E, L)$ models; and dash-double-dotted purple line is the MAMPOSSt model prediction (neglecting velocity errors). It is clear that the LOSVD is significantly non-Gaussian with fat tails across the entire range of radii. The DF-based models are able to capture this behaviour, while the MAMPOSSt method reproduces the trend qualitatively but not in detail, underlining the limitations of using the Gaussian assumption even for the local (not projected) velocity distribution. Grey-shaded region indicates the range of radii used for the LOSVD in the rightmost panel. Centre panel: radial profile of the full LOS velocity dispersion σ_{full} (dashed blue line) and the width of the best-fitting Gaussian σ_{Gauss} (dot-dashed green line). The difference between the two curves indicates the non-Gaussian shape of the LOSVD: The width of the best-fitting Gaussian is comparable to the width of the main peak of the LOSVD, but is significantly smaller than the true second moment of the LOSVD, which is heavily influenced by its tails. Red points with error bars are the binned measured values of the Gaussian approximation to the LOSVD in the 10^4 -star mock data set. Right-hand panel: LOSVD in the penultimate bin (the range of radii indicated by the shaded grey region in the other panels). Solid magenta curve is the true LOSVD; dashed blue curve is a Gaussian profile with the width given by the full second moment of the LOSVD σ_{full} (the quantity that enters the Jeans equations); dot-dashed green curve is the best-fitting Gaussian with width σ_{Gauss} . Neither is a good approximation to the actual LOSVD, which has prominent fat tails.

comparable results). All three Jeans models constrain the LOS and radial and tangential dispersion profiles as in Read & Steger (2017), while the AGAMA DF method uses the 5D phase-space data. As can be seen in Fig. 6, most methods now recover both $\rho(r)$ and $\beta(r)$ within their quoted 95 per cent confidence intervals, although some biases still remain. GRAVSPHERE underestimates $\rho(r)$ at large radii, while DISCRETEJAM overestimates $\rho(r)$ at small radii for the PlumCoreOM mock. AGAMA $f(\mathbf{J})$ and GRAVSPHERE produce less radially anisotropic $\tilde{\beta}$ profiles at large radii for the PlumCuspOM mock, and AGAMA $f(\mathbf{J})$ models are slightly radially biased in the centre. MAMPOSSt obtains a good recovery of $\rho(r)$ and the correct shape for $\tilde{\beta}(r)$, but has $\tilde{\beta}(r)$ biased low at small radii in PlumCuspOM. None the less, with data of this quality all methods are able to distinguish the cusped and cored mocks at high confidence.

5 DISCUSSION AND CONCLUSIONS

We have shown that all four mass modelling methods considered in this paper, using just LOS velocity data, are able to recover both the density and velocity anisotropy as a function of radius within their 95 per cent confidence intervals over the radial range $0.25 < R/R_{1/2} < 4$, for spherically symmetric mock stellar systems, provided that the mocks are isotropic or tangentially anisotropic. However, strong radial anisotropy at large radii presents a more challenging test. Only methods that utilize some information about the shape of the DF are able to recover the density and velocity anisotropy profiles of these mocks. GRAVSPHERE achieves this by using the two fourth-order ‘VSPs’ (Merrifield & Kent 1990); AGAMA achieves it by directly fitting a DF; and MAMPOSSt achieves it by projecting an assumed local Gaussian velocity DF along the LOS. To illustrate this, in Fig. 7

we show the radial profiles of LOS velocity dispersion and kurtosis κ , as well as the LOSVD in the outer parts, for the PlumCoreOM model. Notice that the profiles are substantially non-Gaussian (fat-tailed) across the entire range of radii, indicated by an elevated value of κ . The DF-based AGAMA models are able to capture this behaviour, while the projected Jeans equations used in the DISCRETEJAM method, which uses only the second moment of the DF, assuming a Gaussian LOSVD, become biased. Also, MAMPOSSt predicts too low and high values of kurtosis at small and large radii, respectively, explaining its respective underestimate and overestimate of β at small and large radii (right-hand panels of Fig. 3).

Adding internal proper motion data for 1000 tracer stars, most methods recovered both $\rho(r)$ and $\beta(r)$ within their 95 per cent confidence intervals over the radial range $0.25 < R/R_{1/2} < 4$, albeit with some small biases at the largest and smallest radii. (GRAVSPHERE, in particular, underestimated the density for $R > 2R_{1/2}$ on these tests.) These findings are in good agreement with previous work (e.g. Strigari et al. 2007; Read & Steger 2017), demonstrating the value of obtaining proper motion data for significant numbers of individual stars in nearby dwarf galaxies. This is just beginning to become possible now with the advent of combined *Hubble Space Telescope* and *Gaia* proper motions (Massari et al. 2018, 2020; Vitral & Mamon 2020), but really large data sets will have to wait for the upcoming *Nancy Grace Roman Space Telescope* (Sanderson et al. 2017) and proposed space astrometry missions like *Theia* (Theia Collaboration 2017).

We conclude that breaking the mass–anisotropy degeneracy is crucial for obtaining an unbiased measurement of the density profile and velocity anisotropy of spherical stellar systems. Previous work has focused on achieving this using multiple tracer populations

with different scale lengths (e.g. Battaglia et al. 2008; Walker & Peñarrubia 2011; Amorisco & Evans 2012; Read & Steger 2017). While this has been shown to work well, it can only be applied to systems that have distinct populations. In this paper, we have focused instead on modelling single tracer population data. In this case, with only LOS velocity data, we have shown that the degeneracy can be broken by using higher order ‘VSPs’, by directly fitting a global DF or by self-consistently projecting an assumed local velocity DF along the LOS. We have also uncovered interesting differences even between rather similar-looking methodologies, highlighting the utility of performing detailed tests on mock data and exploring different mass modelling approaches, as we have done here.

Finally, we note that all of the tests in this paper assumed perfect data with small (2 km s^{-1}) velocity errors. Already this was challenging for some methods. Real stellar systems will have additional uncertainties from binary star and foreground contamination (e.g. Walker & Peñarrubia 2011; Read et al. 2018), disequilibrium due to tides (e.g. Kowalczyk et al. 2013; Ural et al. 2015; Read et al. 2018; Genina et al. 2020), rotation (e.g. Watkins et al. 2013; Zhu et al. 2016), departures from spherical symmetry (e.g. Kowalczyk et al. 2013; Laporte et al. 2013; Mamon et al. 2013; Read & Steger 2017; Genina et al. 2020; Hayashi et al. 2020), and inconsistency between the tracer density and kinematic measurements (e.g. Read 2014). Some of these problems can be ameliorated with better data, for example, repeat measurements of individual stars to explore binary contamination (e.g. Koposov et al. 2011; Spencer et al. 2018), metallicity measurements to improve foreground separation, and having a sufficient number of unbiased stars with kinematics that the photometric and kinematic samples are identical. However, some problems like tides will remain, even with exquisite data (e.g. Kowalczyk et al. 2013; Ural et al. 2015). We will explore these issues further in future work.

ACKNOWLEDGEMENTS

We would like to thank the anonymous referee for a constructive and thorough report that improved the paper. JIR would like to acknowledge support from STFC consolidated grant ST/M000990/1 and the MERAC foundation. GAM thanks the French Programme National de Cosmologie et Galaxies (PNCG) of CNRS/INSU with INP and IN2P3, co-funded by CEA and CNES, for financial support of a workshop at IAP during which this work was finalized. EV and PD acknowledge support from the European Research Council (ERC) Horizon 2020 programme under grants 321067 (EV and PD) and 308024 (EV). LLW acknowledges support provided by NASA through *HST* grants AR-14322 and AR-15055, from the Space Telescope Science Institute, which is operated by the Association of Universities for Research in Astronomy, Inc., under NASA contract NAS 5-26555, and from the ERC Horizon 2020 programme under grant agreement no. 724857 (Consolidator Grant ArcheoDyn).

This research has made use of ASTROPY,⁷ a community-developed core PYTHON package for astronomy (Astropy Collaboration 2013), PYNBODY⁸ for the simulation analysis (Pontzen et al. 2013), EMCEE⁹ (Foreman-Mackey et al. 2013), and COSMOMC¹⁰ (Lewis & Bridle 2002) for MCMC sampling, as well as NASA’s Astrophysics Data System.

⁷<http://www.astropy.org>

⁸<https://github.com/pynbody/pynbody>

⁹<https://github.com/dfm/emcee>

¹⁰<https://cosmologist.info/cosmomc/>

DATA AVAILABILITY

The data underlying this article will be shared on reasonable request to the corresponding author. All of the mock data tests can be found on the *Gaia* Challenge wiki site: <http://astrowiki.ph.surrey.ac.uk/dokuwiki/> (under the ‘Spherical & Triaxial’ suite tab). A public version of GRAVSPHERE is available at <https://github.com/AnnaGenina/pyGravSphere>. The AGAMA library, together with the complete PYTHON program performing the DF fitting for this study, is available at <http://agama.software>. A PYTHON package MGETOOLS for manipulating MGEs is available at <http://www.github.com/lauralwatkins/mgetools>.

REFERENCES

- Amorisco N. C., Evans N. W., 2012, *MNRAS*, 419, 184
 An J. H., Evans N. W., 2006, *ApJ*, 642, 752
 Astropy Collaboration, 2013, *A&A*, 558, A33
 Battaglia G., Helmi A., Tolstoy E., Irwin M., Hill V., Jablonka P., 2008, *ApJ*, 681, L13
 Bellini A. et al., 2014, *ApJ*, 797, 115
 Binney J., Mamon G. A., 1982, *MNRAS*, 200, 361
 Binney J., Tremaine S., 2008, *Galactic Dynamics*, 2nd edn., Princeton Univ. Press, Princeton, NJ
 Bonnavard V. et al., 2015, *MNRAS*, 453, 849
 Cappellari M., 2002, *MNRAS*, 333, 400
 Cappellari M., 2008, *MNRAS*, 390, 71
 Cappellari M., 2015, preprint ([arXiv:1504.05533](https://arxiv.org/abs/1504.05533))
 Cappellari M. et al., 2012, *Nature*, 484, 485
 Chiappo A., Cohen-Tanugi J., Conrad J., Strigari L. E., Anderson B., Sánchez-Conde M. A., 2017, *MNRAS*, 466, 669
 Cuddeford P., 1991, *MNRAS*, 253, 414
 Dehnen W., 2009, *MNRAS*, 395, 1079
 Diakogiannis F. I., Lewis G. F., Ibata R. A., Guglielmo M., Wilkinson M. I., Power C., 2019, *MNRAS*, 482, 3356
 Eggen O. J., Lynden-Bell D., Sandage A. R., 1962, *ApJ*, 136, 748
 Emsellem E., Monnet G., Bacon R., 1994, *A&A*, 285, 723
 Foreman-Mackey D., Hogg D. W., Lang D., Goodman J., 2013, *PASP*, 125, 306
 Garbari S., Read J. I., Lake G., 2011, *MNRAS*, 416, 2318
 Genina A., Fairbairn M., 2016, *MNRAS*, 463, 3630
 Genina A. et al., 2020, *MNRAS*, 498, 144
 Geringer-Sameth A., Koushiappas S. M., Walker M. G., 2015, *Phys. Rev. D*, 91, 083535
 Gregory A. L., Collins M. L. M., Read J. I., Irwin M. J., Ibata R. A., Martin N. F., McConnachie A. W., Weisz D. R., 2019, *MNRAS*, 485, 2010
 Hayashi K., Chiba M., Ishiyama T., 2020, *ApJ*, 904, 45
 Hubble E. P., 1926, *ApJ*, 64, 321
 Hénault-Brunet V., Gieles M., Sollima A., Watkins L. L., Zocchi A., Claydon I., Pancino E., Baumgardt H., 2019, *MNRAS*, 483, 1400
 Jeans J. H., 1922, *MNRAS*, 82, 122
 Kamann S. et al., 2018, *MNRAS*, 473, 5591
 Koposov S. E. et al., 2011, *ApJ*, 736, 146
 Kowalczyk K., Łokas E. L., Kazantzidis S., Mayer L., 2013, *MNRAS*, 431, 2796
 Laporte C. F. P., Walker M. G., Peñarrubia J., 2013, *MNRASL*, 433, L54
 Lewis A., Bridle S., 2002, *Phys. Rev. D*, 66, 103511
 Limousin M., Morandi A., Sereno M., Meneghetti M., Ettori S., Bartelmann M., Verdugo T., 2013, *Space Sci. Rev.*, 177, 155
 Mamon G. A., Biviano A., Boué G., 2013, *MNRAS*, 429, 3079
 Mamon G. A., Cava A., Biviano A., Moretti A., Poggianti B., Bettoni D., 2019, *A&A*, 631, A131
 Mamon G. A., Łokas E. L., 2005, *MNRAS*, 363, 705
 Massari D., Breddels M. A., Helmi A., Posti L., Brown A. G. A., Tolstoy E., 2018, *Nat. Astron.*, 2, 156
 Massari D., Helmi A., Mucciarelli A., Sales L. V., Spina L., Tolstoy E., 2020, *A&A*, 633, A36

- McConnachie A. W., Côté P., 2010, *ApJ*, 722, L209
- McMillan P. J., Binney J. J., 2013, *MNRAS*, 433, 1411
- Merrifield M. R., Kent S. M., 1990, *AJ*, 99, 1548
- Merritt D., 1985, *AJ*, 90, 1027
- Merritt D., 1987, *ApJ*, 313, 121
- Napolitano N. R., Pota V., Romanowsky A. J., Forbes D. A., Brodie J. P., Foster C., 2014, *MNRAS*, 439, 659
- Noyola E., Gebhardt K., Bergmann M., 2008, *ApJ*, 676, 1008
- Osipkov L. P., 1979, *Pisma Astron. Zh.*, 5, 77 (English Translation in *Sov. Astron. Lett.*, 5, 42)
- Plummer H. C., 1911, *MNRAS*, 71, 460
- Pontzen A., Roškar R., Stinson G., Woods R., 2013, Pynbody: N-Body/SPH Analysis for Python, Astrophysics Source Code Library, record ascl:1305.002
- Posti L., Binney J., Nipoti C., Ciotti L., 2015, *MNRAS*, 447, 3060
- Read J. I., 2014, *J. Phys. G Nucl. Phys.*, 41, 063101
- Read J. I., Steger P., 2017, *MNRAS*, 471, 4541
- Read J. I., Walker M. G., Steger P., 2018, *MNRAS*, 481, 860
- Read J. I., Walker M. G., Steger P., 2019, *MNRAS*, 484, 1401
- Read J. I., Wilkinson M. I., Evans N. W., Gilmore G., Kleyna J. T., 2006a, *MNRAS*, 367, 387
- Read J. I., Wilkinson M. I., Evans N. W., Gilmore G., Kleyna J. T., 2006b, *MNRAS*, 366, 429
- Richardson T., Fairbairn M., 2014, *MNRAS*, 441, 1584
- Robotham A. et al., 2010, *Publ. Astron. Soc. Aust.*, 27, 76
- Rojas-Niño A., Read J. I., Aguilar L., Delorme M., 2016, *MNRAS*, 459, 3349
- Sanchis T., Łokas E. L., Mamon G. A., 2004, *MNRAS*, 347, 1198
- Sanders J. L., Evans N. W., 2017, *MNRAS*, 472, 2670
- Sanderson R. E. et al., 2017, *J. Astron. Telesc. Instrum. Syst.*, 5, 044005
- Spencer M. E., Mateo M., Olszewski E. W., Walker M. G., McConnachie A. W., Kirby E. N., 2018, *AJ*, 156, 257
- Strigari L. E., Bullock J. S., Kaplinghat M., 2007, *ApJ*, 657, L1
- Syer D., Tremaine S., 1996, *MNRAS*, 282, 223
- Theia Collaboration, 2017, preprint ([arXiv:1707.01348](https://arxiv.org/abs/1707.01348))
- Ural U., Wilkinson M. I., Read J. I., Walker M. G., 2015, *Nat. Commun.*, 6, 7599
- van der Marel R. P., 1994, *MNRAS*, 270, 271
- van der Marel R. P., Anderson J., 2010, *ApJ*, 710, 1063
- Vasiliev E., 2019, *MNRAS*, 482, 1525
- Verolme E. K. et al., 2002, *MNRAS*, 335, 517
- Vitral E., Mamon G. A., 2020, A&A, in press ([arXiv:2010.05532](https://arxiv.org/abs/2010.05532))
- Walker M. G., Mateo M., Olszewski E. W., 2009, *AJ*, 137, 3100
- Walker M. G., Peñarrubia J., 2011, *ApJ*, 742, 20
- Watkins L. L., van der Marel R. P., Bellini A., Anderson J., 2015a, *ApJ*, 812, 149
- Watkins L. L., van der Marel R. P., Bellini A., Anderson J., 2015b, *ApJ*, 803, 29
- Watkins L. L., van de Ven G., den Brok M., van den Bosch R. C. E., 2013, *MNRAS*, 436, 2598
- White R. E., Shawl S. J., 1987, *ApJ*, 317, 246
- Wojtak R., Łokas E. L., Mamon G. A., Gottlöber S., 2009, *MNRAS*, 399, 812
- York D. G. et al., 2000, *AJ*, 120, 1579
- Zhao H., 1996, *MNRAS*, 278, 488
- Zhu L., van de Ven G., Watkins L. L., Posti L., 2016, *MNRAS*, 463, 1117
- Zocchi A., Gieles M., Hénault-Brunet V., 2017, *MNRAS*, 468, 4429

APPENDIX A: RESULTS FOR THE REMAINDER OF THE SPHERICAL MOCKS

For completeness, in this appendix we show the spherically averaged density profile for the remainder of the spherical mocks with 1000 tracer stars, the ‘NonPlum’ models (Fig. A1).

As can be seen, the results are broadly consistent with those for the similar ‘Plum’ mocks, with DISCRETEJAM showing a bias towards cuspy, tangentially anisotropic models, particularly for NonPlumCoreOm, while MAMPOSST shows an even stronger cuspy bias for NonPlumCoreIso. As discussed in Sections 4 and 5, this owes to the mass–anisotropy degeneracy.

Similarly to the PlumCuspOm mock, GRAVSPHERE and DISCRETEJAM fall off too steeply at large radii for NonPlumCuspOm; however, MAMPOSST and AGAMA models also show a similar, albeit less severe, bias.

Interestingly, all of the models except DISCRETEJAM show a slight bias towards cores in the innermost region ($0.25R_{1/2}$) for the NonPlumCuspIso mock. DISCRETEJAM does not show this bias, but this is because it shows a bias instead towards tangentially anisotropic models. (Tangentially anisotropic models require a steeper density profile to match the data that, in this case, drives a better match with the input model.) MAMPOSST (and DISCRETEJAM to a lesser extent) finds instead an even steeper inner density profile than the NFW model used to build this mock. By contrast, for the NonPlumCuspIso mock, both GRAVSPHERE and AGAMA are consistent with the input isotropic DF within their 95 per cent confidence intervals, while MAMPOSST produces tangential orbits at all radii (not shown for brevity). As such, the bias towards cores in the NonPlumCuspIso mock does not owe to the mass–anisotropy degeneracy. We speculate that it owes instead to the cuspy light profile in this mock yielding a poorer radial sampling of the stellar kinematics. (For a fixed number of tracers, cuspiest light profiles will have relatively fewer sample points at large radii.) This warrants further investigation in future work. However, we note that it is unlikely to impact most real stellar systems, since these typically have a much shallower inner tracer-density profile than the rather extreme ‘NonPlum’ mocks explored here (see e.g. Read et al. 2019, for nearby dwarf galaxies).

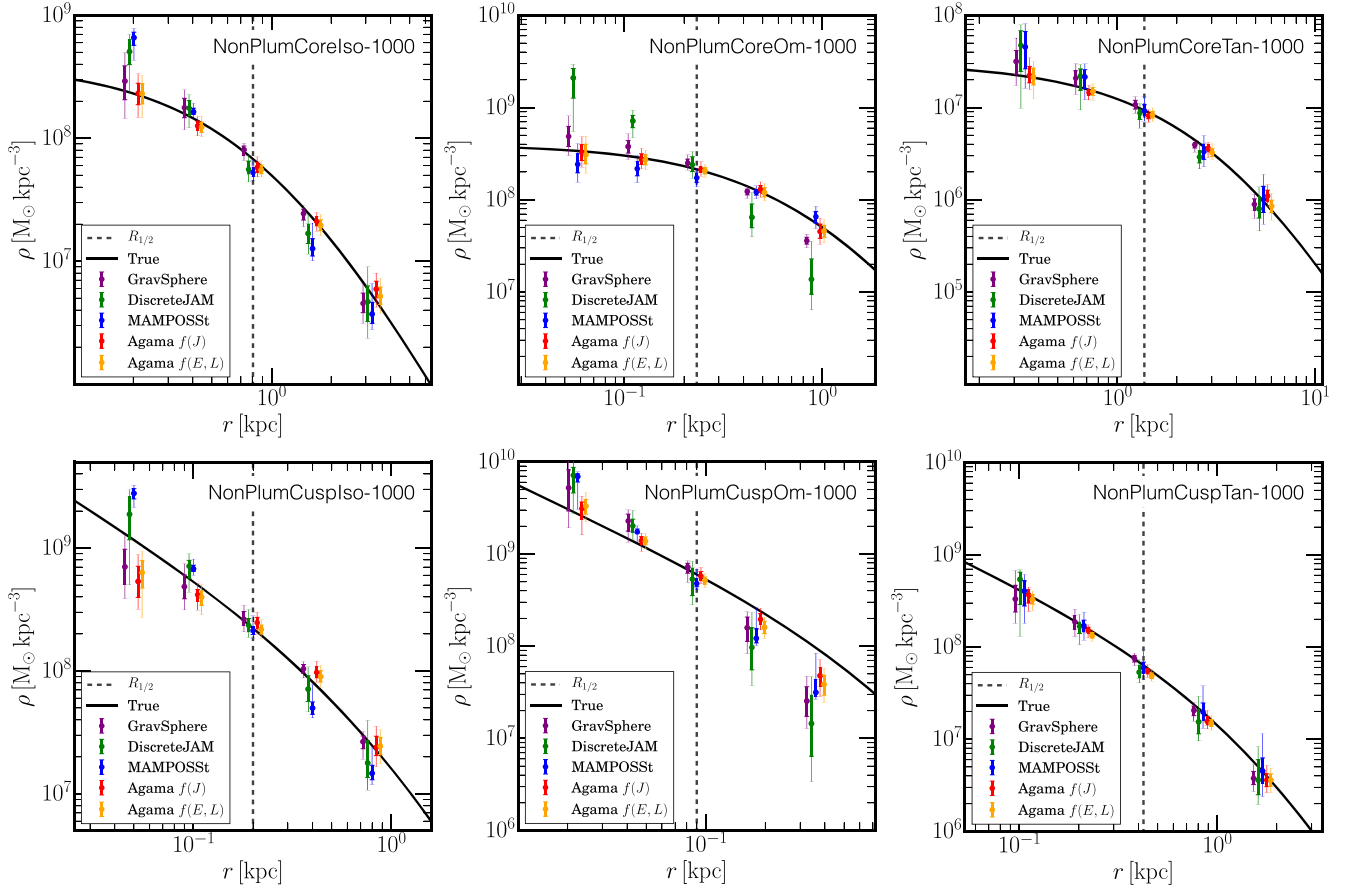


Figure A1. As Fig. 1 but for the ‘NonPlum’ spherical mocks, as marked on the panels.

This paper has been typeset from a \LaTeX file prepared by the author.